Structure

Structural characterization of the POTRA domains from *A. baumannii* reveals new conformations in BamA

Graphical abstract

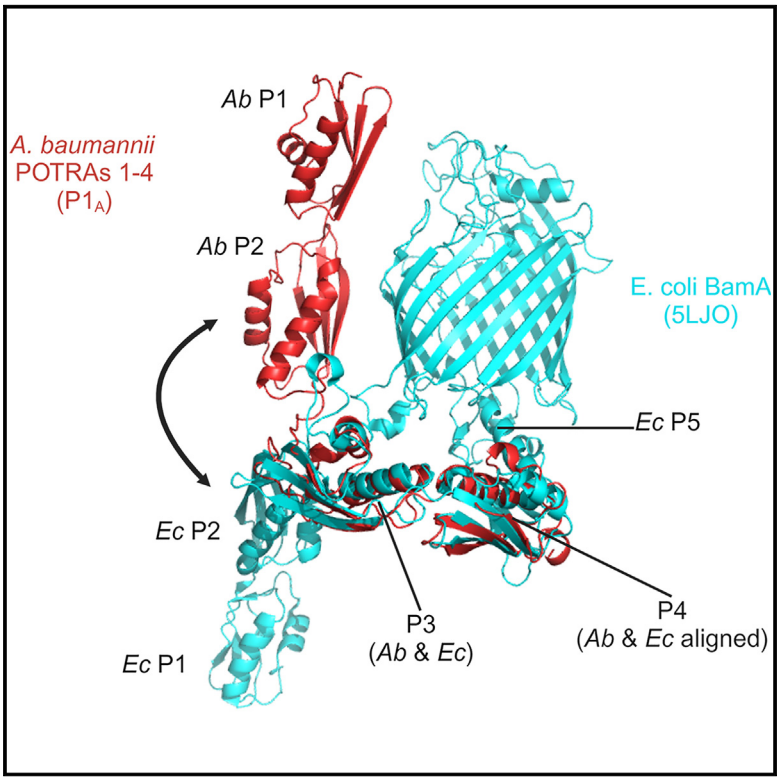

Authors

Claire Overly Cottom, Robert Stephenson, Dante Ricci, Lixinhao Yang, James C. Gumbart, Nicholas Noinaj

Correspondence

nnoinaj@purdue.edu

In brief

In *A. baumannii*, BamA has an N-terminal periplasmic domain consisting of five tandem POTRA domains. Overly Cottom et al. determined crystal structures of AbBamA POTRAs 1–4, revealing new conformations that are rotated by ~180°, indicating even more conformational plasticity than has been observed previously and offering a possible explanation for surface exposure of accessory proteins.

Highlights

- The POTRA domains of BamA are known to be flexible
- Crystal structures of *A. baumannii* BamA POTRA domains reveal novel conformations
- MD simulations and SAXS data are consistent with the crystal structures
- These new conformations may explain how Bam components become surface exposed

Cottom et al., 2024, Structure *32*, 2038–2048
November 7, 2024 © 2024 Elsevier Inc. All rights reserved, including those for text and data mining, AI training, and similar technologies.
https://doi.org/10.1016/j.str.2024.08.013

CellPress

CellPress

Structure

Article

Structural characterization of the POTRA domains from *A. baumannii* reveals new conformations in BamA

Claire Overly Cottom,[1,8] Robert Stephenson,[1,8] Dante Ricci,[2,7] Lixinhao Yang,[3] James C. Gumbart,[3,4] and Nicholas Noinaj[1,5,6,9,*]

[1]Department of Biological Sciences, Purdue University, West Lafayette, IN, USA
[2]Achaogen, Inc., South San Francisco, CA, USA
[3]School of Chemistry and Biochemistry, Georgia Institute of Technology, Atlanta, GA, USA
[4]School of Physics, Georgia Institute of Technology, Atlanta, GA, USA
[5]Markey Center for Structural Biology, Purdue University, West Lafayette, IN, USA
[6]Purdue Institute of Inflammation, Immunology and Infectious Disease, Purdue University, West Lafayette, IN, USA
[7]Present address: Biosciences and Biotechnology Division, Lawrence Livermore National Laboratory, Livermore, CA, USA
[8]These authors contributed equally
[9]Lead contact
*Correspondence: nnoinaj@purdue.edu
https://doi.org/10.1016/j.str.2024.08.013

SUMMARY

Recent studies have demonstrated BamA, the central component of the β-barrel assembly machinery (BAM), as an important therapeutic target to combat infections caused by *Acinetobacter baumannii* and other Gram-negative pathogens. Homology modeling indicates BamA in *A. baumannii* consists of five polypeptide transport-associated (POTRA) domains and a β-barrel membrane domain. We characterized the POTRA domains of BamA from *A. baumannii* in solution using size-exclusion chromatography small angle X-ray scattering (SEC-SAXS) analysis and determined crystal structures in two conformational states that are drastically different than those previously observed in BamA from other bacteria, indicating that the POTRA domains are even more conformationally dynamic than has been observed previously. Molecular dynamics simulations of the POTRA domains from *A. baumannii* and *Escherichia coli* allowed us to identify key structural features that contribute to the observed novel states. Together, these studies expand on our current understanding of the conformational plasticity within BamA across differing bacterial species.

INTRODUCTION

Acinetobacter baumannii is a Gram-negative pathogen that causes a variety of infections in humans including pneumonia, bloodstream infections, wound infections, urinary tract infections, and meningitis.[1] *A. baumannii* is a significant cause of hospital-derived infections and it has a unique ability to persist on surfaces, which makes the emergence of drug-resistant strains particularly problematic.[2–7] In 2019, the World Health Organization designated carbapenem-resistant *A. baumannii* as an urgent threat,[8] necessitating the rapid development of new treatments to combat *A. baumannii* infections.

A. baumannii, like all other Gram-negative bacteria, is characterized by the presence of an inner membrane (IM) and an outer membrane (OM) separated by the periplasm and sandwiching the peptidoglycan layer. The OM uniquely contains a host of β-barrel outer membrane proteins (OMPs) that perform many cellular functions including nutrient import, cell signaling, and adhesion.[9–14] Nascent OMPs are trafficked across the IM by the Sec translocon, shuttled across the periplasm with the help of periplasmic chaperones, and are folded and inserted into the OM by the β-barrel assembly machinery (BAM) complex.[11,15–17] In *Escherichia coli*, the BAM complex consists of BamA, which is itself an OMP, and BamB, C, D, and E, which are soluble periplasmic domains that are attached to the inner leaflet of the OM by lipid anchors.[18–22] Both BamA and BamD are required for viability in *E. coli*,[23] and are highly conserved among other Gram-negative bacteria.[18,24–26] There is, however, variability in the number and type of BAM complex lipoprotein subunits present across different bacterial species.[18,24–28] Due to its essential role in the cell, the BAM complex has recently become an emerging target for the development of novel antimicrobial therapeutics targeting Gram-negative bacteria.[13,29–33]

The *A. baumannii* genome codes for homologs of all five canonical BAM complex subunits (BamA-E) present in *E. coli*, so

 © 2024 Elsevier Inc.
All rights are reserved, including those for text and data mining, AI training, and similar technologies.

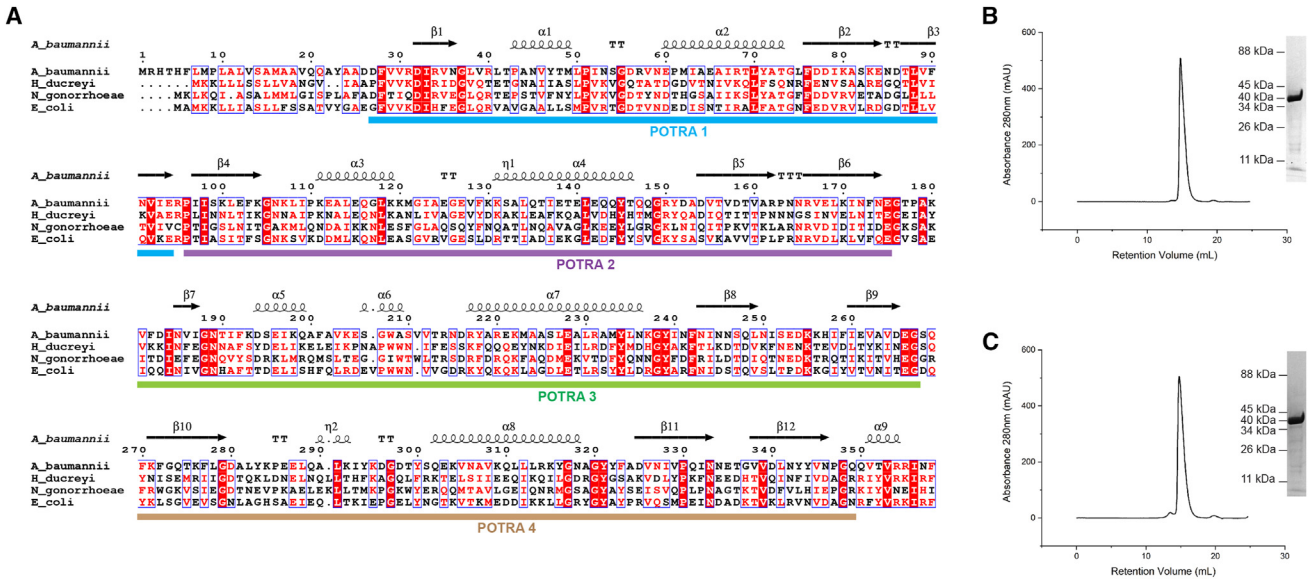

Figure 1. Sequence comparison of POTRAs 1–4 and purification of this domain from *A. baumannii*

(A) Alignment of the *Ab*BamA POTRAs 1–4 amino acid sequence with other structurally characterized orthologs of BamA. The secondary structure of BamA POTRAs 1–4 from *A. baumannii* is shown based on our studies here. The boundaries for each POTRA domain are indicated in blue, purple, green, and brown. (B) The SEC profile from native and selenomethionine substituted (C) *Ab*BamA POTRAs 1–4 showing a pure sample running at ~40 kDa (expected mass is 41 kDa including the His tag).

the BAM complex might represent one possible target for novel antimicrobial therapeutics capable of treating *Acinetobacter* infections. Recent studies have shown that recombinant *A. baumannii* BamA can effectively be used to immunize mice against infection with *A. baumannii*.[13,34] However, no structural characterization of *A. baumannii* BamA, or any other BAM complex component, has been performed to date. Elucidation of the structure of the BAM complex and its individual components from *Acinetobacter* would provide the structural basis for targeting this complex for new therapeutics against pathogenic *Acinetobacter*.

BamA is the central component of the BAM complex and performs the insertase activity mediating OMP biogenesis.[35–41] BamA is composed of an N-terminal periplasmic domain consisting of five polypeptide transport associated (POTRA) domains with a C-terminal β-barrel domain that is inserted in the OM. The barrel domain consists of 16 β-strands and has a lateral seam joining strands 1 and 16 forming the final barrel shape of the protein.[39] BamA functions by inducing local disruptions with the OM to allow OMPs to insert into the membrane. Additionally, the barrel of BamA has been shown to serve as a "template" for which the new OMP nucleates and forms.[42–44] The periplasmic POTRA domains of BamA interact directly with the accessory lipoproteins to form an extensive assembly beneath the BamA barrel.[45–49]

The number of POTRA domains present across bacterial species is variable, as *Fusobacterium nucleatum* BamA is predicted to contain four; *Neisseria gonorrhoeae*, *E. coli*, and *A. baumannii* contain five; and *Myxococcus xanthus* contains seven.[24,27,28] Additionally, the minimal number of POTRA domains that are essential for viability also varies among Gram-negative species.[50] For example, POTRA 3–5 are essential in *E. coli*,[23,41] while only POTRA 5 is essential in *N. meningitidis*.[51] In *E. coli* BAM, BamB interacts with POTRAs 2 and 3 along the hinge between them[45–47,52] and BamD interacts primarily with POTRA 5 and minimally with POTRA 2.[45–47,53]

The POTRA domains provide the scaffold for the association of the Bam lipoproteins to assemble into the higher order complex.[45–47] POTRA domains typically have a conserved secondary structure, with a $\beta_1\alpha_1\alpha_2\beta_2\beta_3$ topology, despite sequence divergence.[41,54,55] Each POTRA repeat within *E. coli* BamA was found to be structurally conserved, except for a β-bulge present in POTRA 3.[41,55] Conformational flexibility in the POTRA domains is important for mediating changes in the full complex that assist in initiation and folding of the new OMPs. It has been postulated that the POTRA domains may serve as a chaperone to assist the unfolded OMPs with pre-forming β-strands through β-templating using the exposed edges of strands present in the POTRA domains.[54,56]

Here we report the expression, purification, and structural characterization of the POTRA domains of BamA from *A. baumannii* (*Ab*BamA) and do a structural comparison to POTRA domains from other bacterial species. We characterized the POTRA 1–4 domains of *Ab*BamA in solution using size-exclusion chromatography small angle X-ray scattering (SEC-SAXS) analysis, molecular dynamics (MD) simulations, and determined crystal structures in two conformational states. These conformational states are drastically different from those previously observed in BamA from other bacteria, indicating that the POTRA domains are even more conformationally dynamic than has been observed previously. Our study further expands on our current understanding of the plasticity within BamA and BAM during OMP biogenesis.

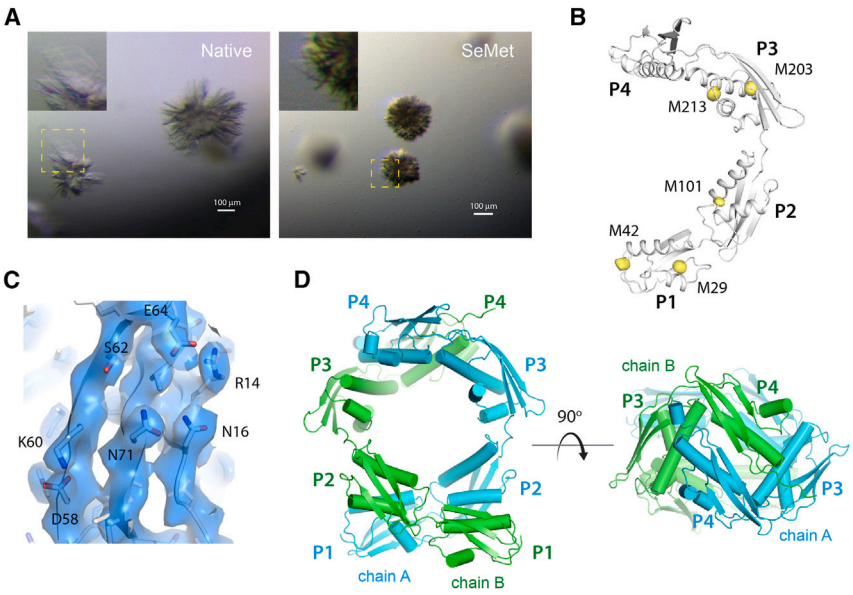

Figure 2. Structure determination of *Ab*BamA POTRAs 1–4

(A) *Ab*BamA POTRAs 1–4 crystals showing small thin finely stacked plates.

(B) The structure of *Ab*BamA POTRAs 1–4 highlighting the selenomethionine sites used for phasing.

(C) Representative electron density (blue isosurface; 1 σ) for the *Ab*BamA POTRAs 1–4 structure.

(D) The asymmetric unit of the structure in space group $P3_221$ showing two molecules with pseudo 2-fold non-crystallographic symmetry. Orthogonal views are shown.

RESULTS

Structure determination of the POTRA 1–4 domains from *A. baumannii*

The N-terminal POTRA 1–4 domains of BamA (residues 25–355) from *A. baumannii* (strain 19606) (*Ab*BamA) were cloned into the pHisParallel2 vector and expressed in BL21(DE3) cells. (Figure 1A). *Ab*BamA POTRAs 1–4 were purified by nickel affinity chromatography, followed by removal of the His-tag by cleavage with TEV protease, and then size-exclusion chromatography (SEC) as a final purification step. Purified *Ab*BamA POTRAs 1–4 migrated at an expected size of ~41 kDa on an SDS-PAGE gel (Figures 1B and 1C). For single-wavelength anomalous dispersion (SAD) phasing experiments, expression was performed in the methionine-auxotroph B834(DE3) cells that were grown in SelenoMethionine Medium Complete (Molecular Dimensions). Selenomethionine-substituted BamA POTRAs 1–4 was purified as described previously. Both native and selenomethionine-substituted *Ab*BamA POTRAs 1–4 were concentrated to 10 mg/mL for crystallization.

High-throughput broad matrix crystallization screening was performed using hanging drop method (1:1 protein:well solution ratio) and all lead conditions looped directly from the trays and screened for diffraction quality. Initial crystallization conditions consisted of 100 mM citric acid, pH 4.0, and 800 mM ammonium sulfate for both native and selenomethionine-substituted (Se-met) *Ab*BamA POTRAs 1–4 (Figure 2A). *Ab*BamA POTRAs 1–4 crystals grew as thin fragile plates. Despite extensive optimization methods including seeding, all *Ab*BamA POTRAs 1–4 crystals were clusters of thin plates that were difficult to separate and loop individually. We identified ethylene glycol in our additive screen as an additive that allowed us to obtain some larger, single thin crystal plates (Figure S1A). The best native crystals were grown in 100 mM citric acid, pH 3.8, 630 mM ammonium sulfate, and 13% ethylene glycol. Additionally, lowering the protein concentration of *Ab*BamA POTRAs 1–4 in the drop from 10 mg/mL to 5 mg/mL for native sample or 2.5 mg/mL for the Se-met sample also helped produce crystals more suitable for looping. To confirm that the crystals we obtained were indeed BamA POTRAs 1–4, we washed them briefly in a mix of well solution and sample buffer, redissolved in LDS loading buffer by gentle pipetting, and visualized by SDS-PAGE (not shown). The molecular weight observed for the crystallized protein was ~41 kDa, which matches the molecular weight we observed for purified BamA POTRAs 1–4 after SEC, indicating that the protein crystals obtained were *Ab*BamA POTRAs 1–4.

Data collection was performed at the GM/CA beamline at the Advanced Photon Source and the data processed using HKL2000[57] to space group P1 with unit cell parameters a = 59.93 Å, b = 65.92 Å, c = 87.02 Å, with α = 67.76°, β = 88.28° and γ = 65.82°. Analysis of the processed dataset using Xtriage[58] predicted 3 copies of BamA POTRAs 1–4 per ASU with a Matthews coefficient of 2.6 and a solvent content of 52%. Attempts to use existing structures of POTRA domains as search models, as well as computational models, for molecular replacement for initial phasing were unsuccessful. This was likely due to the elongated and flexible nature of the periplasmic domain itself. We then collected multiple selenium-SAD datasets from a single crystal. The data were again processed in space group P1, but with cell parameters a = 56.52 Å, b = 61.51 Å, c = 85.90 Å, with α = 97.59°, β = 107.35°, and γ = 112.45°; again with 3 copies per ASU predicted with a Matthews coefficient of 2.3 and a solvent content of 46% (Table 1). Attempts at experimental phasing with both Se-SAD and Se-MAD phasing were also unsuccessful. We attributed this again to partially being in space group P1, but mostly due to the observation that the crystal did not appear to be uniformly isotropic, as evidenced by the varying cell parameters from one end of the crystal to the other. Therefore merging multiple datasets was not assisting to amplify the anomalous signal as would typically be the case.

We revisited our initial crystallization screening in hopes that we could find another condition with more favorable packing, but had limited options given that only the current condition produced high-resolution diffraction. Since we could produce the sample at relatively high yields, to overcome this limitation, we performed reductive alkylation of the selenium-substituted sample and rescreened it using broad matrix high-throughput screening. This led to large single crystals in multiple conditions. These crystals were then screened for diffraction quality with one condition, 0.1 M Bis-Tris propane pH 7.0, 1.2 M DL-malic acid,

Table 1. Data collection and refinement statistics

Data collection	Dataset 1	Dataset 2
λ (Å)	0.9793	0.9793
Space group	$P3_221$	P1
a, b, c (Å)	94.9 94.9 220.3	56.52 61.51 85.90
α, β, γ (°)	90 90 120	97.6 107.3 112.4
Resolution (Å)[e]	47.46–2.60 (2.69–2.60)	39.37–2.80 (2.90–2.80)
Completeness (%)[e]	100 (100)	87.0 (88.0)
Redundancy[e]	19.6 (19.8)	2.5 (2.4)
R_{sym}[a,e]	0.114 (1.23)	0.146 (1.32)
I/σ (I)[e]	27.7 (1.7)	10.5 (1.0)
$CC_{1/2}$	0.998 (0.79)	0.992 (0.284)
#Se found	10 sites/ASU	
FOM	0.307	
Bayes-CC	52.46	
Skew	0.20	
Refinement		
Resolution (Å)	47.46–2.60 (2.69–2.60)	39.37–2.78 (2.85–2.78)
No. reflections	35,362 (2,278)	23,193 (1,445)
R^b/R_{free}^c	0.22/0.24	0.24/0.29
RMSDs		
Bonds (Å)	0.004	0.003
Angles (°)	0.78	0.57
No. protein atoms	5,167	4,897
No. waters	41	39
B-factors (Å2)		
Wilson B	78.94	85.99
Protein	79.15	86.20
Waters	56.52	56.19
Ramachandran Analysis[d]		
Favored (%)	97.24	95.25
Allowed (%)	2.45	4.45
Outliers (%)	0.31	0.31
PDB:	9CX5	9CX4

[a] $R_{sym} = \Sigma_{hkl,j}(|I_{hkl}-\langle I_{hkl}\rangle|)/\Sigma_{hkl,j} I_{hkl}$, where $\langle I_{hkl}\rangle$ is the average intensity for a set of j symmetry related reflections and I_{hkl} is the value of the intensity for a single reflection within a set of symmetry-related reflections.
[b] R factor $= \Sigma_{hkl}(||F_o| - |F_c||)/\Sigma_{hkl}|F_o|$ where F_o is the observed structure factor amplitude and F_c is the calculated structure factor amplitude.
[c] $R_{free} = \Sigma_{hkl,T}(||F_o| - |F_c||)/\Sigma_{hkl,T}|F_o|$, where a test set, T (5% of the data), is omitted from the refinement.
[d] Performed using Molprobity within PHENIX.
[e] Indicates statistics for last resolution shell shown in parenthesis.

pH 7.0, producing the best diffraction (Figures S1B and S1C). The data were processed in space group $P3_221$ with cell parameters a = 94.92 Å, b = 94.92 Å, c = 220.30 Å, with α = 90°, β = 90° and γ = 120°; again with 3 copies per ASU predicted with a Matthews coefficient of 2.6 and a solvent content of 52%. Se-SAD phasing was performed using AutoSol in PHENIX[58] that produced an interpretable map (10 Se-sites per ASU with FOM of 0.307, Bayes-CC of 52.5, and Map Skew of 0.2) (Figures 2B and 2C). Using COOT, models of the individual POTRA 1–4 domains could be placed into the density, with a final solution of two molecules being built into the ASU with R_{work} and R_{free} values of 0.22 and 0.25 at a resolution of 2.6 Å (Figure 2D).

Once the Se-SAD structure in space group $P3_221$ was solved, it was used as a starting search model for solving the structure of the selenium-substituted crystals in space group P1 using molecular replacement, which also contained only two molecules in the ASU with R_{work} and R_{free} values of 0.24 and 0.29 at a resolution of 2.78 Å. We then solved the native structure in space group P1 and found the same packing, however, at lower resolution (2.93 Å). Therefore, we only report the highest resolution structure in P1 in our study here.

Structural alignment reveals conformational plasticity in *Ab*BamA POTRAs 1–4

While cell content analysis for both structures predicted three molecules per ASU, only two were observed for each space group (Figures 3A and 3B). A root-mean-square deviation (RMSD) of 3.6 Å was calculated when comparing chain A to chain B in the $P3_221$ structure, where chains A and B refer each to a molecule within the ASU, indicating significant conformational flexibility (Figure 3C). However, an RMSD of 0.7 Å was calculated when comparing chain A to chain B in the P1 structure, where minimal differences were observed between the monomers within the ASU (Figure 3D). When comparing chain A from the P1 space group to chain A and chain B from the $P3_221$ structure, RMSDs of 6.3 Å and 8.5 Å were calculated, respectively (Figures 3E and 3F). This indicated an even larger conformational deviation among the structures in the two space groups. In total, we observed three conformational states: (1) space group P1, chains A and B, (2) space group $P3_221$, chain A, and (3) space group $P3_221$, chain B.

An alignment of both chains of POTRAs 1–4 from space group $P3_221$ with chain A from space group P1 shows significant conformational flexibility, with the structures in P1 being more extended (Figures 4A and 4B). An alignment along POTRAs 3 and 4 of the three conformational states observed in our *Ab*BamA POTRAs 1–4 structures shows ∼45° sweep spanning ∼54 Å of POTRAs 1 and 2 along the hinge between POTRA 2 and 3 (Figure 4B). Comparing these conformations to previously reported structures from *E. coli* revealed conformations not previously observed in the POTRA domains of BamA. Comparing the POTRA domains from *Ab*BamA in space group P1, chain A, to *E. coli* (PDB: 3EFC) shows ∼180° shift of POTRAs 1 and 2, with others ranging from ∼130° to 150° (PDB: 5EKQ, 2QDF, and 2QCZ) (Figure 5A). A similar observation was observed in comparison to the POTRA domains of BamA from *N. gonorrhoeae* (PDB: 4K3B) and *Haemophilus influenzae* (PDB: 6J09) (not shown).

A structural comparison of the individual POTRA domains of BamA from *A. baumannii*, *E. coli*, and *N. gonorrhoeae* shows good pairwise structural agreement for all four POTRA domains with RMSDs ranging from 0.9 to 3.3 Å (Figure S2A; Table S1). The most notable structural difference was found in POTRA 3, where the loop between α1 and α2 has an additional small helix in *A. baumannii* that is absent in both *E. coli* and *N. gonorrhoeae* (Figures S2B and S2C). Importantly, this loop sits at the junction where POTRAs 1 and 2 are shifted in the opposite direction in *E. coli* and *N. gonorrhoeae*, suggesting this loop may be contributing factor leading to the unique conformation observed in *A. baumannii*.

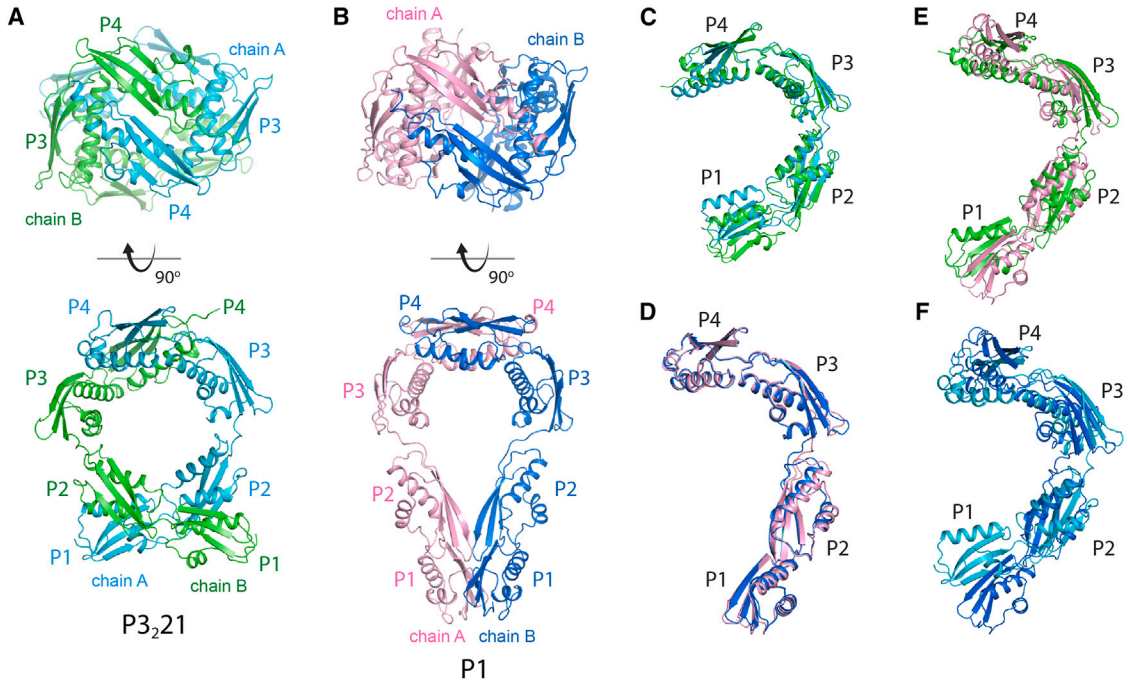

Figure 3. The structures of *Ab*BamA POTRAs 1–4 in condensed and extended conformational states

(A) The assembly of *Ab*BamA POTRAs 1–4 in the asymmetric unit in space group $P3_221$ and P1 (B), both with pseudo 2-fold non-crystallographic symmetry.

(C) A superposition of the two chains in space group $P3_221$ (RMSD value of 3.6 Å) and P1 (D; RMSD value of 0.7 Å). The conformation of the structure in P1 is more extended.

(E) A superposition of chains A (RMSD of 6.3 Å) and B (F; RMSD of 8.5 Å) from each respective space group.

SEC-SAXS authenticates conformational plasticity in *Ab*BamA POTRAs 1–4

To investigate the structure of POTRAs 1–4 in solution, we performed SEC-SAXS at the BioCAT beamline at the Advanced Photon Source (Figure 4C). The scattering curve and Guinier plot indicated an aggregation-free sample with an R_g of 35.0 Å and a D_{max} of 126 Å (Figures 4C and 4D), with an average mass calculation of ~41 kDa (Table 2). These results are consistent with a monomer in solution and with our reported crystal structures that have a max dimension of 110 Å (range from 80 to 110 Å). A Kratky plot is also consistent with a globular folded protein containing an elongated disordered N-terminal linker region (Figure 4E).

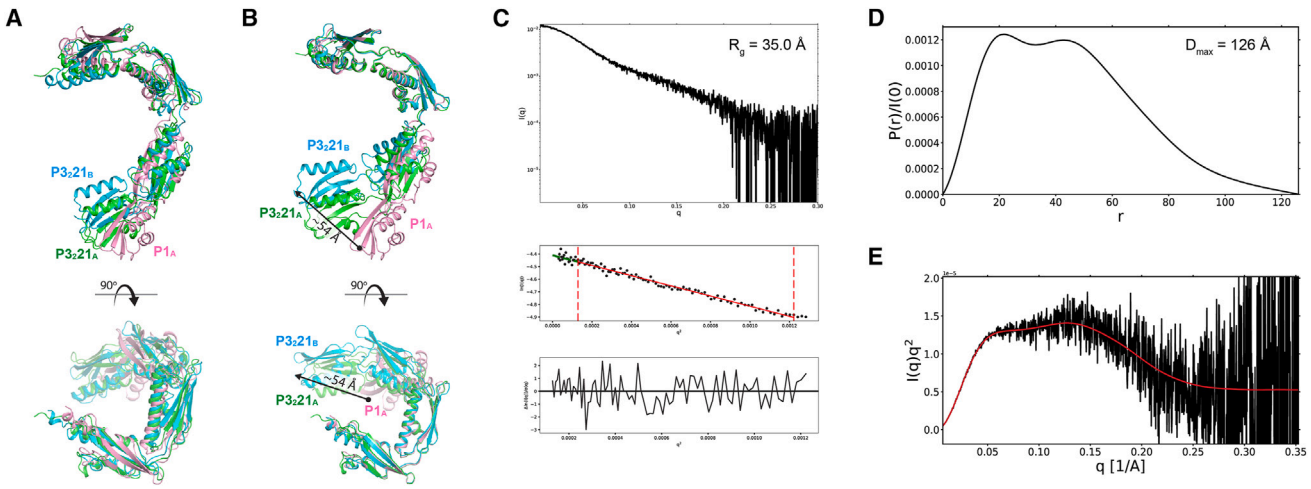

Figure 4. SAXS analysis of *Ab*BamA POTRAs 1–4

(A) An overall superposition of chain A from space group P1 to both chains in space group $P3_221$. Orthogonal views are shown.

(B) The same structural alignment as in (A), yet superimposed along POTRAs 3 and 4, demonstrating a large ~45° swing of POTRAs 1 and 2 moving ~54 Å.

(C) SEC-SAXS analysis of *Ab*BamA POTRAs 1–4 gave an R_g of 35 Å, an average mass of 41.5 kDa, and a D_{max} value of 126 Å (D).

(E) A Kratky plot is consistent with a globular fold containing flexible linkers on its termini.

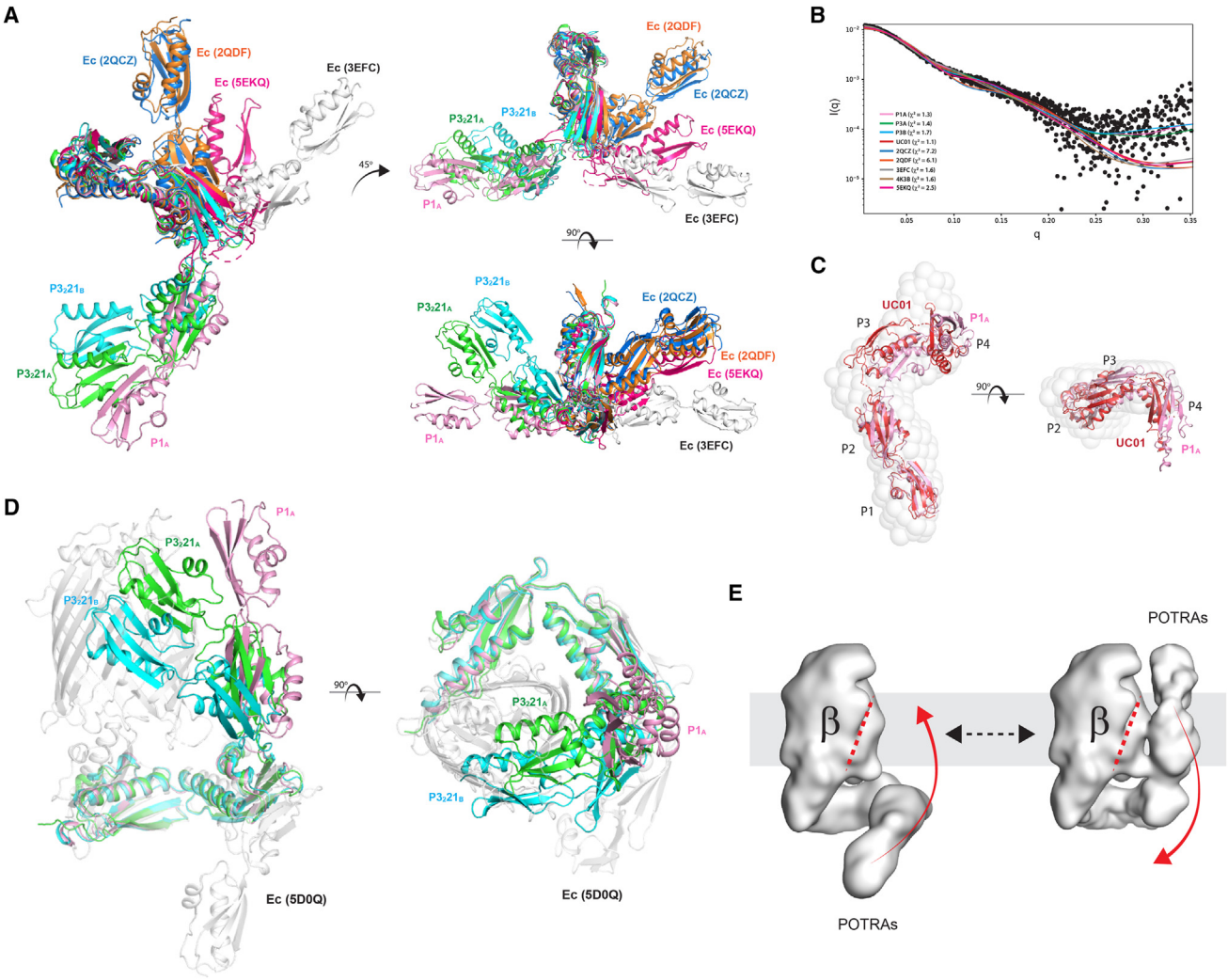

Figure 5. *Ab*BamA POTRA 1–4 reveals new conformations in BamA

(A) A structural alignment of POTRAs 1–4 from *Ab*BamA with *Ec*BamA alone (PDB: 2QCZ, 2QDF, and 3EFC) and *Ec*BamA within the BAM complex (PDB: 5EKQ). The left panel is the same view as in Figures 4A and 4B, while the top-right view is rotated ∼45° from the left view, with the right-bottom being orthogonal to the top-right.

(B) CRYSOL was used to compare calculated scattering curves of the structures from (A) to the experimental scattering curve in Figure 4C. χ^2 values indicate the closest match is chain A from space group P1 of *Ab*BamA POTRAs 1–4 (pink; χ^2 value of 1.3), while the structures for *Ec*BamA have χ^2 values ranging from 1.6–7.2; *Ng*BamA has a χ^2 value of 1.6. SREFLEX was used to improve the fit of chain A from space group P1 of *Ab*BamA POTRAs 1–4, producing UC01 (red), which gave a χ^2 value of 1.1.

(C) A superposition of chain A from space group P1 of *Ab*BamA POTRAs 1–4 (pink) and UC01 (red) with the DAMMIN/IF SAXS envelope.

(D) Modeling the new conformations with the full length *E. coli* BamA structure (PDB: 5D0Q).

(E) A surface depiction of the two conformations from (D), where the POTRA domains are in the periplasm and at the membrane surface.

To determine what conformation was observed in solution, CRYSOL was used to compare calculated scattering curves from the POTRAs 1–4 structures from *Ab*BamA and *Ec*BamA to the experimental SEC-SAXS scattering curve (Figures 5A and 5B). Values for χ^2 ranged from 1.3–1.7 for the *Ab*BamA structures with chain A from space group P1 having the lowest value and therefore most closely matching the observed conformation. Other structures had elevated χ^2 values of 1.6 (PDB: 3EFC and 4K3B), 2.5 (PDB: 5EKQ), 6.1 (PDB: 2QDF), and 7.2 (PDB: 2QCZ), demonstrating the deviation from the conformational states observed in *Ab*BamA. SRE-FLEX was used to optimize the fit of the P1A structure to the experimental SEC-SAXS scattering curve, producing a slightly modified structure (UC01) with a χ^2 value of 1.1. An alignment of the P1A structure, UC01 structure, and the DAMMIF/IN envelope shows good agreement along POTRAs 1–3, with the largest conformational deviation along POTRA 4, suggesting we likely have a mix of conformational states in solution as well (Figure 5C).

MD simulations reveal differences in conformational plasticity between *Ab*BamA and *Ec*BamA POTRAs 1–4

We performed MD simulations for two *Ab*BamA models (chains A and B of the structure solved here) and two *Ec*BamA models (chains A and B of PDB: 2QCZ) to investigate

Table 2. Summary of SEC-SAXS data collection parameters and results

Data Collection	
Instrument/data processing	Advanced Photon Source, BioCAT beamline with Pilatus3 1M detector
Wavelength (Å)	1.0332
Beam size (μm)	~30 × 150
Camera length (m)	3.631
Q measurement range ($Å^{-1}$)	0.0047–0.3525
Exposure time (s)	0.5
Sample configuration	SEC-MALS-SAXS
Sample temperature (°C)	22

Data processing						
		Molecular Weight (kDa)				
Protein Complex	R_g (Å)	V_c	V_p	Bayes	MALS	D_{max} (Å)
*Ab*BamA (POTRA 1–4)	35.0	38.1	46.1	40.2	39.0	126

The POTRA domains 1–4 from *Ab*BamA (without His tag) has a calculated molecular weight of 38 kDa.

the dynamic behavior of both *Ab*BamA and *Ec*BamA POTRA domains (Figure 6A). During the simulations, the POTRAs exhibited significant flexibility. Both *Ab*BamA and *Ec*BamA displayed two types of states: an "open" state, when no hydrogen bonds were formed between POTRAs 1 and 4 (Figures 6B and 6C), and a "closed" state, when stable interactions formed between POTRAs 1 and 4 (Figures 6E and 6F).

The distribution of angles formed by POTRAs 1 and 2, POTRAs 2 and 3, and POTRAs 3 and 4 for both *Ab*BamA and *Ec*BamA were calculated to compare their respective conformations (Figures 6H and 6I). For both *Ab*BamA and *Ec*BamA, the POTRA 1-2 angle distributions are located around 30°–80°, although *Ec*BamA has a narrower distribution. Significant distribution differences were observed for POTRA 2-3 and POTRA 3-4 angles. *Ab*BamA shows two peaks around 50° and 100° for the POTRA 2-3 angle distribution, while *Ec*BamA had a single peak around 115°. Specifically, for *Ab*BamA, the closed state mostly corresponded to the 100° peak, and the open state to the 50° peak. For the POTRA 3-4 angle, *Ab*BamA had one peak near 80°, while *Ec*BamA had two peaks at 60° and 120°, corresponding to the closed and open states, respectively.

The structural differences between *Ab*BamA and *Ec*BamA POTRA domains include a longer α-helix in *Ab*BamA at POTRA 3 (Figure 6A). This steric hindrance directly influenced the dynamics. During simulations, the POTRA 2 domain tended to fold in different directions for *Ab*BamA and *Ec*BamA. For *Ec*BamA, POTRA 2 folded toward the longer α-helix side (Figure 6G), while for *Ab*BamA, it folded toward the shorter α-helix side (Figure 6D). In the *Ab*BamA simulations, stable salt bridges formed by Lys204 on POTRA 3 with Glu142 and Asp154 on POTRA 2 were observed (with occupancies of 47.8% and 34.7%, respectively; Figure S3A), but similar stable hydrogen bonding was not observed in *Ec*BamA simulations.

The shorter helical structure of POTRA 3 in *Ec*BamA provides more flexibility, leading to a larger and more unstable RMSD value compared to *Ab*BamA's POTRA 3 (Figures S3C and S3D). When POTRA 2 folded toward the longer α-helix side, it pushed the α-helix upward to POTRA 4. This movement causes POTRA 4 to orient itself between the two helices of POTRA 3 due to steric hindrance, which prevents it from reaching the closed state (Figure S3B).

In summary, the structural differences between the POTRA 3 domains of *Ec*BamA and *Ab*BamA play a critical role in their dynamic behavior. The binding interactions and steric hindrances contribute to the preferential states observed in *Ab*BamA and *Ec*BamA. *Ec*BamA, characterized by its shorter α-helix, demonstrates greater flexibility and spends a larger proportion of time in the closed state (30.2% for *Ec*BamA is in the close state, compared to 17.5% for *Ab*BamA). In contrast, *Ab*BamA, with its more stable and longer POTRA 3 α-helix, tends to maintain an extended, open conformation.

DISCUSSION

Recent studies reporting the discovery of antimicrobial compounds targeting BamA have established that BAM is an exciting new target for the development of new antibiotics and vaccines against Gram-negative bacterial pathogens. Most functional and structural studies on BAM have been done in *E. coli*, with no structures reported for *A. baumannii*, which is at the top of the CDC's list of urgent threats to public health due to multidrug resistance. To better understand how BAM functions in *A. baumannii*, here we report the structural characterization of the POTRA domains of BamA, the central and essential component of BAM (*Ab*BamA). Our findings reveal new conformations of the POTRA domains that are significantly different than has been previously observed, providing new insights into the flexibility and dynamics of BamA. These new insights may be important for the general function of BamA in all Gram-negative bacteria or may represent a unique feature of BamA in *A. baumannii*.

Previous structural studies of BamA, either alone or within fully assembled BAM, have demonstrated flexibility within the POTRA domains of BamA. The first structures from *E. coli* of the POTRA domains only and the structures of fully assembled BAM highlight this conformational heterogeneity, something that was also observed in *N. gonorrhoeae*, *H. ducreyi*, and *H. influenzae*. Given that the accessory proteins BamB, C, D, and E assemble along the POTRA domains, the conformations of the POTRA domains are thought to be important in (1) mediating substrate interaction with BAM during biogenesis and (2) transducing conformational changes in the periplasmic region to the β-barrel of BamA that sits in the membrane. These conformational changes in the β-barrel domain of BamA are essential for the function of BAM and for turning on and off OMP biogenesis.

X-ray crystal and cryoelectron microscopy (cryo-EM) structures of BAM and BamA have demonstrated a range of conformations in the POTRA domains of BamA. These conformations are more restricted when bound with the accessory proteins; however, significant changes are present even then as demonstrated by the inward-open and outward-open states that BAM has been observed to adopt. These findings have been fully supported by computational studies that have been performed both in detergent and in membranes. The structures of POTRAs 1–4 of *Ab*BamA reported here reveal that the POTRA domains of BamA have even more

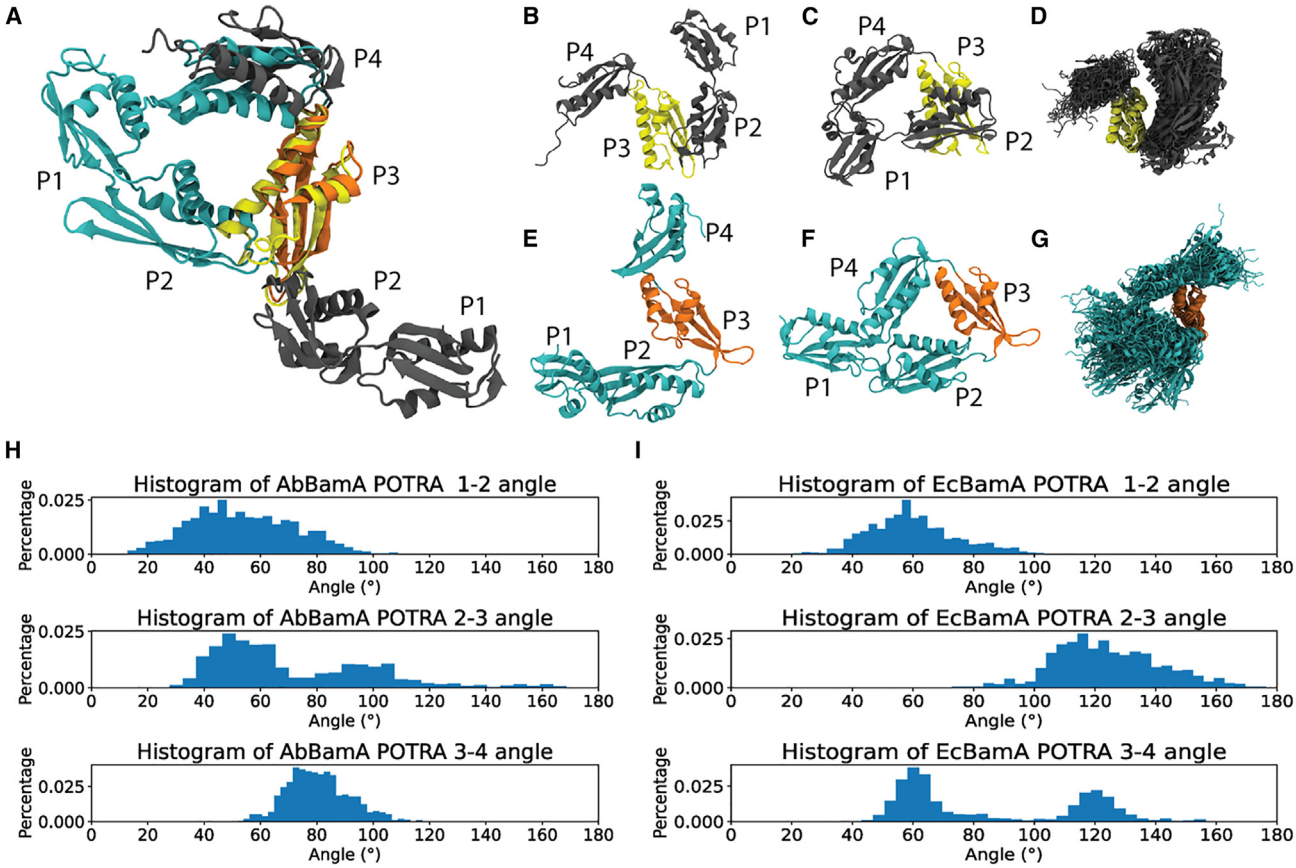

Figure 6. The conformation of *Ab*BamA and *Ec*BamA POTRA 1–4 in MD simulations

*Ab*BamA POTRAs 1, 2, and 4 are shown in dark gray, and POTRA3 is in yellow. *Ec*BamA POTRAs 1, 2, and 4 are shown in blue and POTRA 3 is in orange.

(A) The initial conformation for *Ab*BamA and *Ec*BamA POTRAs.

(B and C) Snapshots of "open" (B) and "closed" states (C) of *Ab*BamA.

(E and F) Snapshots of "open" (B) and "closed" states (C) of *Ec*BamA.

(D and G) Overlapping conformations of *Ab*BamA (D) and *Ec*BamA (G) chain A during the trajectories, with one snapshot every 20 ns. Structures are aligned based on POTRA 3 β-sheet structures in (A), (D), and (G).

(H and I) Distribution of angles formed by different POTRA domains of *Ab*BamA (H) and *Ec*BamA (I).

conformational freedom than has been previously observed experimentally or computationally. A comparison of POTRAs 1 and 2 in relation to POTRAs 3 and 4 shows a rotational movement ranging from ∼130° to 180° compared to *Ec*BamA, sweeping a distance of ∼117–136 Å (Figure 5D). The exact role of these new conformations of BamA remains to be determined, but could explain multiple reports of Bam accessory proteins (BamC, BamD, and BamE) being surface exposed.[59,60] In previously reported conformations, the POTRAs are fully within the periplasm. In our studies here, the POTRAs are projected up toward the membrane where they could assist in presenting the bound accessory proteins to the surface, although exactly how they would traverse the membrane is unknown (Figure 5E). MD simulations revealed that conformational differences arise in part due to a longer α-helix in POTRA 3 and salt bridges formed between POTRAs 2 and 3, which stabilize the conformations observed in the *Ab*BamA POTRAs 1-4 crystal structures (Figures S3A and S3B). Another contributing factor for these conformations may be mechanistic differences between *E. coli* and *A. baumannii*. Given the varied conformations identified here (Figures 6H and 6I), it is likely that BamA POTRA domains from other species will also display distinct conformational distributions.

RESOURCE AVAILABILITY

Lead contact

Further information and requests for resources and reagents should be directed to and will be fulfilled by the lead contact, Nicholas Noinaj (nnoinaj@purdue.edu).

Materials availability

Primary data and other materials are available upon reasonable request to the lead contact.

Data and code availability

- Data generated in this study are available upon reasonable request from the lead contact. Crystal structures have been deposited to the PDB. These are publicly available as of the date of publication. Accession numbers are listed in the key resources table.
- This paper does not report any original code.
- Any additional information required to reanalyze the data reported in this paper is available from the lead contact upon request.

ACKNOWLEDGMENTS

We would like to thank the Noinaj lab for critical reading of the manuscript and for providing comments and discussions. We would like to acknowledge funding support from Achaogen and from NIH grants 1R01GM127884 (N.N.), 1R01GM127896 (N.N.), and R01GM123169 (J.C.G.), which helped support this work. C.O.C. was supported as a trainee through the T32 Drug Discovery in Infectious Disease Program (T32AI148103) and through a Bilsland Dissertation Fellowship (Department of Biological Science, Purdue University). A special thanks to Steve Wilson for maintaining and managing our computing resources; and the staff at the BioCAT and GM/CA beamlines at the Advanced Photon Source at Argonne National Laboratory for their assistance with data collection. The BioCAT resources are supported by grant P30 GM138395 from the NIGMS of the NIH; use of the Pilatus 3 1M detector was provided by grant 1S10OD018090 from NIGMS. GM/CA@APS has been funded by the National Cancer Institute (ACB-12002) and the National Institute of General Medical Sciences (AGM-12006, P30GM138396). This research used resources of the Advanced Photon Source, a U.S. Department of Energy (DOE) Office of Science User Facility operated for the DOE Office of Science by Argonne National Laboratory under Contract No. DE-AC02-06CH11357. The Eiger 16M detector at GM/CA-XSD was funded by NIH grant S10 OD012289. Computational resources were provided through ACCESS (grant TG-MCB130173), which is supported by National Science Foundation grants 2138259, 2138286, 2138307, 2137603, and 2138296.

AUTHOR CONTRIBUTIONS

N.N. and D.R. conceived the study; D.R. provided funding for the project through Achaogen; R.S. cloned, expressed, purified, and crystallized all the constructs; N.N., R.S., and C.O.C collected the diffraction data and solved the structures; N.N. collected the SAXS data with assistance from the staff at BioCAT and N.N., R.S., and C.O.C. analyzed the data; L.Y. and J.C.G. performed the MD simulations studies; N.N., R.S., and C.O.C. assembled the manuscript with contributions from all authors.

DECLARATION OF INTERESTS

The authors declare no competing interests.

STAR★METHODS

Detailed methods are provided in the online version of this paper and include the following:

- KEY RESOURCES TABLE
- EXPERIMENTAL MODEL AND STUDY PARTICIPANT DETAILS
- METHOD DETAILS
  - Cloning
  - Protein expression and purification
  - Reductive alkylation of selenomethionine-substituted BamA polypeptide transport associated 1-4
  - Crystallization
  - Data collection and structure determination
  - Size-exclusion chromatography small angle X-Ray scattering
  - Molecular dynamics simulations
- QUANTIFICATION AND STATISTICAL ANALYSIS

SUPPLEMENTAL INFORMATION

Supplemental information can be found online at https://doi.org/10.1016/j.str.2024.08.013.

Received: January 5, 2024
Revised: July 17, 2024
Accepted: August 22, 2024
Published: September 17, 2024

REFERENCES

1. Peleg, A.Y., Seifert, H., and Paterson, D.L. (2008). Acinetobacter baumannii: emergence of a successful pathogen. Clin. Microbiol. Rev. *21*, 538–582. https://doi.org/10.1128/CMR.00058-07.
2. Morris, F.C., Dexter, C., Kostoulias, X., Uddin, M.I., and Peleg, A.Y. (2019). The Mechanisms of Disease Caused by Acinetobacter baumannii. Front. Microbiol. *10*, 1601. https://doi.org/10.3389/fmicb.2019.01601.
3. Elbehiry, A., Marzouk, E., Moussa, I., Mushayt, Y., Algarni, A.A., Alrashed, O.A., Alghamdi, K.S., Almutairi, N.A., Anagreyyah, S.A., Alzahrani, A., et al. (2023). The Prevalence of Multidrug-Resistant Acinetobacter baumannii and Its Vaccination Status among Healthcare Providers. Vaccines (Basel) *11*, 1171. https://doi.org/10.3390/vaccines11071171.
4. Rodriguez-Martinez, J.M., Nordmann, P., Ronco, E., and Poirel, L. (2010). Extended-spectrum cephalosporinase in Acinetobacter baumannii. Antimicrob. Agents Chemother. *54*, 3484–3488. https://doi.org/10.1128/AAC.00050-10.
5. Howard, A., O'Donoghue, M., Feeney, A., and Sleator, R.D. (2012). Acinetobacter baumannii: an emerging opportunistic pathogen. Virulence *3*, 243–250. https://doi.org/10.4161/viru.19700.
6. Asif, M., Alvi, I.A., and Rehman, S.U. (2018). Insight into Acinetobacter baumannii: pathogenesis, global resistance, mechanisms of resistance, treatment options, and alternative modalities. Infect. Drug Resist. *11*, 1249–1260. https://doi.org/10.2147/IDR.S166750.
7. Ahmad, S., Ranaghan, K.E., and Azam, S.S. (2019). Combating tigecycline resistant Acinetobacter baumannii: A leap forward towards multi-epitope based vaccine discovery. Eur. J. Pharmaceut. Sci. *132*, 1–17. https://doi.org/10.1016/j.ejps.2019.02.023.
8. CDC (2019). Antibiotic Resistance Threats in the United States.
9. Fairman, J.W., Noinaj, N., and Buchanan, S.K. (2011). The structural biology of β-barrel membrane proteins: a summary of recent reports. Curr. Opin. Struct. Biol. *21*, 523–531. https://doi.org/10.1016/j.sbi.2011.05.005.
10. Lin, J., Huang, S., and Zhang, Q. (2002). Outer membrane proteins: key players for bacterial adaptation in host niches. Microb. Infect. *4*, 325–331. https://doi.org/10.1016/s1286-4579(02)01545-9.
11. Rollauer, S.E., Sooreshjani, M.A., Noinaj, N., and Buchanan, S.K. (2015). Outer membrane protein biogenesis in Gram-negative bacteria. Philos. Trans. R. Soc. Lond. B Biol. Sci. *370*, 20150023. https://doi.org/10.1098/rstb.2015.0023.
12. Uppalapati, S.R., Sett, A., and Pathania, R. (2020). The Outer Membrane Proteins OmpA, CarO, and OprD of Acinetobacter baumannii Confer a Two-Pronged Defense in Facilitating Its Success as a Potent Human Pathogen. Front. Microbiol. *11*, 589234. https://doi.org/10.3389/fmicb.2020.589234.
13. Singh, R., Capalash, N., and Sharma, P. (2017). Immunoprotective potential of BamA, the outer membrane protein assembly factor, against MDR Acinetobacter baumannii. Sci. Rep. *7*, 12411. https://doi.org/10.1038/s41598-017-12789-3.
14. Nie, D., Hu, Y., Chen, Z., Li, M., Hou, Z., Luo, X., Mao, X., and Xue, X. (2020). Outer membrane protein A (OmpA) as a potential therapeutic target for Acinetobacter baumannii infection. J. Biomed. Sci. *27*, 26. https://doi.org/10.1186/s12929-020-0617-7.
15. Ricci, D.P., and Silhavy, T.J. (2012). The Bam machine: A molecular cooper. Biochim. Biophys. Acta *1818*, 1067–1084. https://doi.org/10.1016/j.bbamem.2011.08.020.
16. Noinaj, N., Gumbart, J.C., and Buchanan, S.K. (2017). The beta-barrel assembly machinery in motion. Nat. Rev. Microbiol. *15*, 197–204. https://doi.org/10.1038/nrmicro.2016.191.
17. Knowles, T.J., Scott-Tucker, A., Overduin, M., and Henderson, I.R. (2009). Membrane protein architects: the role of the BAM complex in outer membrane protein assembly. Nat. Rev. Microbiol. *7*, 206–214. https://doi.org/10.1038/nrmicro2069.

18. Anwari, K., Webb, C.T., Poggio, S., Perry, A.J., Belousoff, M., Celik, N., Ramm, G., Lovering, A., Sockett, R.E., Smit, J., et al. (2012). The evolution of new lipoprotein subunits of the bacterial outer membrane BAM complex. Mol. Microbiol. *84*, 832–844. https://doi.org/10.1111/j.1365-2958.2012.08059.x.

19. Fussenegger, M., Facius, D., Meier, J., and Meyer, T.F. (1996). A novel peptidoglycan-linked lipoprotein (ComL) that functions in natural transformation competence of Neisseria gonorrhoeae. Mol. Microbiol. *19*, 1095–1105.

20. Sklar, J.G., Wu, T., Gronenberg, L.S., Malinverni, J.C., Kahne, D., and Silhavy, T.J. (2007). Lipoprotein SmpA is a component of the YaeT complex that assembles outer membrane proteins in Escherichia coli. Proc. Natl. Acad. Sci. USA *104*, 6400–6405. https://doi.org/10.1073/pnas.0701579104.

21. Fardini, Y., Chettab, K., Grépinet, O., Rochereau, S., Trotereau, J., Harvey, P., Amy, M., Bottreau, E., Bumstead, N., Barrow, P.A., and Virlogeux-Payant, I. (2007). The YfgL lipoprotein is essential for type III secretion system expression and virulence of Salmonella enterica Serovar Enteritidis. Infect. Immun. *75*, 358–370. https://doi.org/10.1128/IAI.00716-06.

22. Okuda, S., and Tokuda, H. (2011). Lipoprotein sorting in bacteria. Annu. Rev. Microbiol. *65*, 239–259. https://doi.org/10.1146/annurev-micro-090110-102859.

23. Wu, T., Malinverni, J., Ruiz, N., Kim, S., Silhavy, T.J., and Kahne, D. (2005). Identification of a Multicomponent Complex Required for Outer Membrane Biogenesis in Escherichia coli. Cell *121*, 235–245. https://doi.org/10.1016/j.cell.2005.02.015.

24. Webb, C.T., Heinz, E., and Lithgow, T. (2012). Evolution of the beta-barrel assembly machinery. Trends Microbiol. *20*, 612–620. https://doi.org/10.1016/j.tim.2012.08.006.

25. Jiang, J.H., Tong, J., Tan, K.S., and Gabriel, K. (2012). From evolution to pathogenesis: the link between beta-barrel assembly machineries in the outer membrane of mitochondria and gram-negative bacteria. Int. J. Mol. Sci. *13*, 8038–8050. https://doi.org/10.3390/ijms13078038.

26. Ulrich, T., and Rapaport, D. (2015). Biogenesis of beta-barrel proteins in evolutionary context. Int. J. Med. Microbiol. *305*, 259–264. https://doi.org/10.1016/j.ijmm.2014.12.009.

27. Heinz, E., and Lithgow, T. (2014). A comprehensive analysis of the Omp85/TpsB protein superfamily structural diversity, taxonomic occurrence, and evolution. Front. Microbiol. *5*, 370. https://doi.org/10.3389/fmicb.2014.00370.

28. Heinz, E., Selkrig, J., Belousoff, M.J., and Lithgow, T. (2015). Evolution of the Translocation and Assembly Module (TAM). Genome Biol. Evol. *7*, 1628–1643. https://doi.org/10.1093/gbe/evv097.

29. Imai, Y., Meyer, K.J., Iinishi, A., Favre-Godal, Q., Green, R., Manuse, S., Caboni, M., Mori, M., Niles, S., Ghiglieri, M., et al. (2019). A new antibiotic selectively kills Gram-negative pathogens. Nature *576*, 459–464. https://doi.org/10.1038/s41586-019-1791-1.

30. Kaur, H., Jakob, R.P., Marzinek, J.K., Green, R., Imai, Y., Bolla, J.R., Agustoni, E., Robinson, C.V., Bond, P.J., Lewis, K., et al. (2021). The antibiotic darobactin mimics a beta-strand to inhibit outer membrane insertase. Nature *593*, 125–129. https://doi.org/10.1038/s41586-021-03455-w.

31. Hart, E.M., Mitchell, A.M., Konovalova, A., Grabowicz, M., Sheng, J., Han, X., Rodriguez-Rivera, F.P., Schwaid, A.G., Malinverni, J.C., Balibar, C.J., et al. (2019). A small-molecule inhibitor of BamA impervious to efflux and the outer membrane permeability barrier. Proc. Natl. Acad. Sci. USA *116*, 21748–21757. https://doi.org/10.1073/pnas.1912345116.

32. Overly Cottom, C., Stephenson, R., Wilson, L., and Noinaj, N. (2023). Targeting BAM for Novel Therapeutics against Pathogenic Gram-Negative Bacteria. Antibiotics *12*, 679. https://doi.org/10.3390/antibiotics12040679.

33. Storek, K.M., Auerbach, M.R., Shi, H., Garcia, N.K., Sun, D., Nickerson, N.N., Vij, R., Lin, Z., Chiang, N., Schneider, K., et al. (2018). Monoclonal antibody targeting the beta-barrel assembly machine of Escherichia coli is bactericidal. Proc. Natl. Acad. Sci. USA *115*, 3692–3697. https://doi.org/10.1073/pnas.1800043115.

34. Vieira de Araujo, A.E., Conde, L.V., da Silva Junior, H.C., de Almeida Machado, L., Lara, F.A., Chapeaurouge, A., Pauer, H., Pires Hardoim, C.C., Martha Antunes, L.C., D'Alincourt Carvalho-Assef, A.P., and Moreno Senna, J.P. (2021). Cross-reactivity and immunotherapeutic potential of BamA recombinant protein from Acinetobacter baumannii. Microb. Infect. *23*, 104801. https://doi.org/10.1016/j.micinf.2021.104801.

35. Tokuda, H. (2009). Biogenesis of outer membranes in Gram-negative bacteria. Biosci. Biotechnol. Biochem. *73*, 465–473. https://doi.org/10.1271/bbb.80778.

36. Bennion, D., Charlson, E.S., Coon, E., and Misra, R. (2010). Dissection of beta-barrel outer membrane protein assembly pathways through characterizing BamA POTRA 1 mutants of Escherichia coli. Mol. Microbiol. *77*, 1153–1171. https://doi.org/10.1111/j.1365-2958.2010.07280.x.

37. Tommassen, J. (2010). Assembly of outer-membrane proteins in bacteria and mitochondria. Microbiology *156*, 2587–2596. https://doi.org/10.1099/mic.0.042689-0.

38. Noinaj, N., Kuszak, A.J., Balusek, C., Gumbart, J.C., and Buchanan, S.K. (2014). Lateral Opening and Exit Pore Formation Are Required for BamA Function. Structure *22*, 1055–1062. https://doi.org/10.1016/j.str.2014.05.008.

39. Noinaj, N., Kuszak, A.J., Gumbart, J.C., Lukacik, P., Chang, H., Easley, N.C., Lithgow, T., and Buchanan, S.K. (2013). Structural insight into the biogenesis of beta-barrel membrane proteins. Nature *501*, 385–390. https://doi.org/10.1038/nature12521.

40. Malinverni, J.C., Werner, J., Kim, S., Sklar, J.G., Kahne, D., Misra, R., and Silhavy, T.J. (2006). YfiO stabilizes the YaeT complex and is essential for outer membrane protein assembly in Escherichia coli. Mol. Microbiol. *61*, 151–164. https://doi.org/10.1111/j.1365-2958.2006.05211.x.

41. Kim, S., Malinverni, J.C., Sliz, P., Silhavy, T.J., Harrison, S.C., and Kahne, D. (2007). Structure and Function of an Essential Component of the Outer Membrane Protein Assembly Machine. Science *317*, 961–964. https://doi.org/10.1126/science.1143993.

42. Wu, R., Bakelar, J.W., Lundquist, K., Zhang, Z., Kuo, K.M., Ryoo, D., Pang, Y.T., Sun, C., White, T., Klose, T., et al. (2021). Plasticity within the barrel domain of BamA mediates a hybrid-barrel mechanism by BAM. Nat. Commun. *12*, 7131. https://doi.org/10.1038/s41467-021-27449-4.

43. Doyle, M.T., and Bernstein, H.D. (2019). Bacterial outer membrane proteins assemble via asymmetric interactions with the BamA beta-barrel. Nat. Commun. *10*, 3358. https://doi.org/10.1038/s41467-019-11230-9.

44. Tomasek, D., Rawson, S., Lee, J., Wzorek, J.S., Harrison, S.C., Li, Z., and Kahne, D. (2020). Structure of a nascent membrane protein as it folds on the BAM complex. Nature *583*, 473–478. https://doi.org/10.1038/s41586-020-2370-1.

45. Bakelar, J., Buchanan, S.K., and Noinaj, N. (2016). The structure of the beta-barrel assembly machinery complex. Science *351*, 180–186. https://doi.org/10.1126/science.aad3460.

46. Gu, Y., Li, H., Dong, H., Zeng, Y., Zhang, Z., Paterson, N.G., Stansfeld, P.J., Wang, Z., Zhang, Y., Wang, W., and Dong, C. (2016). Structural basis of outer membrane protein insertion by the BAM complex. Nature *531*, 64–69. https://doi.org/10.1038/nature17199.

47. Han, L., Zheng, J., Wang, Y., Yang, X., Liu, Y., Sun, C., Cao, B., Zhou, H., Ni, D., Lou, J., et al. (2016). Structure of the BAM complex and its implications for biogenesis of outer-membrane proteins. Nat. Struct. Mol. Biol. *23*, 192–196. https://doi.org/10.1038/nsmb.3181.

48. Iadanza, M.G., Higgins, A.J., Schiffrin, B., Calabrese, A.N., Brockwell, D.J., Ashcroft, A.E., Radford, S.E., and Ranson, N.A. (2016). Lateral opening in the intact beta-barrel assembly machinery captured by cryo-EM. Nat. Commun. *7*, 12865. https://doi.org/10.1038/ncomms12865.

49. Shen, C., Chang, S., Luo, Q., Chan, K.C., Zhang, Z., Luo, B., Xie, T., Lu, G., Zhu, X., Wei, X., et al. (2023). Structural basis of BAM-mediated outer membrane beta-barrel protein assembly. Nature *617*, 185–193. https://doi.org/10.1038/s41586-023-05988-8.

50. Diederichs, K.A., Buchanan, S.K., and Botos, I. (2021). Building Better Barrels - beta-barrel Biogenesis and Insertion in Bacteria and Mitochondria. J. Mol. Biol. *433*, 166894. https://doi.org/10.1016/j.jmb.2021.166894.

51. Bos, M.P., Robert, V., and Tommassen, J. (2007). Functioning of outer membrane protein assembly factor Omp85 requires a single POTRA domain. EMBO Rep. *8*, 1149–1154. https://doi.org/10.1038/sj.embor.7401092.

52. Jansen, K.B., Baker, S.L., and Sousa, M.C. (2015). Crystal structure of BamB bound to a periplasmic domain fragment of BamA, the central component of the beta-barrel assembly machine. J. Biol. Chem. *290*, 2126–2136. https://doi.org/10.1074/jbc.M114.584524.

53. Bergal, H.T., Hopkins, A.H., Metzner, S.I., and Sousa, M.C. (2016). The Structure of a BamA-BamD Fusion Illuminates the Architecture of the beta-Barrel Assembly Machine Core. Structure *24*, 243–251. https://doi.org/10.1016/j.str.2015.10.030.

54. Knowles, T.J., Jeeves, M., Bobat, S., Dancea, F., McClelland, D., Palmer, T., Overduin, M., and Henderson, I.R. (2008). Fold and function of polypeptide transport-associated domains responsible for delivering unfolded proteins to membranes. Mol. Microbiol. *68*, 1216–1227. https://doi.org/10.1111/j.1365-2958.2008.06225.x.

55. Gatzeva-Topalova, P.Z., Walton, T.A., and Sousa, M.C. (2008). Crystal Structure of YaeT: Conformational Flexibility and Substrate Recognition. Structure *16*, 1873–1881. https://doi.org/10.1016/j.str.2008.09.014.

56. Ma, X., Wang, Q., Li, Y., Tan, P., Wu, H., Wang, P., Dong, X., Hong, L., and Meng, G. (2019). How BamA recruits OMP substrates via poly-POTRAs domain. Faseb. J. *33*, 14690–14702. https://doi.org/10.1096/fj.201900681RR.

57. Otwinowski, Z., and Minor, W. (1997). Processing of X-Ray Diffraction Data Collected in Oscillation Mode in Methods in Enzymology (Academic Press), pp. 307–326.

58. Adams, P.D., Afonine, P.V., Bunkóczi, G., Chen, V.B., Davis, I.W., Echols, N., Headd, J.J., Hung, L.W., Kapral, G.J., Grosse-Kunstleve, R.W., et al. (2010). PHENIX: a comprehensive Python-based system for macromolecular structure solution. Acta Crystallogr. D Biol. Crystallogr. *66*, 213–221. https://doi.org/10.1107/S0907444909052925.

59. Webb, C.T., Selkrig, J., Perry, A.J., Noinaj, N., Buchanan, S.K., and Lithgow, T. (2012). Dynamic association of BAM complex modules includes surface exposure of the lipoprotein BamC. J. Mol. Biol. *422*, 545–555. https://doi.org/10.1016/j.jmb.2012.05.035.

60. Sikora, A.E., Wierzbicki, I.H., Zielke, R.A., Ryner, R.F., Korotkov, K.V., Buchanan, S.K., and Noinaj, N. (2018). Structural and functional insights into the role of BamD and BamE within the beta-barrel assembly machinery in Neisseria gonorrhoeae. J. Biol. Chem. *293*, 1106–1119. https://doi.org/10.1074/jbc.RA117.000437.

61. Emsley, P., Lohkamp, B., Scott, W.G., and Cowtan, K. (2010). Features and development of Coot. Acta Crystallogr. D Biol. Crystallogr. *66*, 486–501. https://doi.org/10.1107/S0907444910007493.

62. Hopkins, J.B., Gillilan, R.E., and Skou, S. (2017). BioXTAS RAW: improvements to a free open-source program for small-angle X-ray scattering data reduction and analysis. J. Appl. Crystallogr. *50*, 1545–1553. https://doi.org/10.1107/S1600576717011438.

63. Manalastas-Cantos, K., Konarev, P.V., Hajizadeh, N.R., Kikhney, A.G., Petoukhov, M.V., Molodenskiy, D.S., Panjkovich, A., Mertens, H.D.T., Gruzinov, A., Borges, C., et al. (2021). ATSAS 3.0: expanded functionality and new tools for small-angle scattering data analysis. J. Appl. Crystallogr. *54*, 343–355. https://doi.org/10.1107/S1600576720013412.

64. Phillips, J.C., Hardy, D.J., Maia, J.D.C., Stone, J.E., Ribeiro, J.V., Bernardi, R.C., Buch, R., Fiorin, G., Hénin, J., Jiang, W., et al. (2020). Scalable molecular dynamics on CPU and GPU architectures with NAMD. J. Chem. Phys. *153*, 044130. https://doi.org/10.1063/5.0014475.

65. Huang, J., Rauscher, S., Nawrocki, G., Ran, T., Feig, M., de Groot, B.L., Grubmüller, H., and MacKerell, A.D., Jr. (2017). CHARMM36m: an improved force field for folded and intrinsically disordered proteins. Nat. Methods *14*, 71–73. https://doi.org/10.1038/nmeth.4067.

66. Balusek, C., Hwang, H., Lau, C.H., Lundquist, K., Hazel, A., Pavlova, A., Lynch, D.L., Reggio, P.H., Wang, Y., and Gumbart, J.C. (2019). Accelerating Membrane Simulations with Hydrogen Mass Repartitioning. J. Chem. Theor. Comput. *15*, 4673–4686. https://doi.org/10.1021/acs.jctc.9b00160.

STAR★METHODS

KEY RESOURCES TABLE

REAGENT or RESOURCE	SOURCE	IDENTIFIER
Bacterial and virus strains		
E. coli strain BL21(DE3)	New England Biolabs	C2527H
E. coli strain B834(DE3)	EMD Millipore	69041
Chemicals, peptides, and recombinant proteins		
2xYT Media	Research Products International	X15600-5000.0
Selenomethionine Medium Complete	Molecular Dimensions	MD12-500
Ampicillin sodium salt	Fisher Bioreagents	BP1760-25
Isopropyl β-D-1-thiogalactopyranoside (IPTG)	Gold Biotechnology	P-470-25
β-mercaptoethanol (BME)	Fisher Chemical	O3446I-100
Phenylmethylsulfonyl fluoride (PMSF)	Gold Biotechnology	P-470-25
DNAseI	Gold Biotechnology	D-300-1
Imidazole	Fisher Chemical	O3196-500
Dithiothreitol (DTT)	GoldBio	DTT100
Ethylenediaminetetraacetic acid (EDTA)	Fisher Chemical	S311-500
Hydrochloric acid (HCl)	Fisher Chemical	A144-212
Formaldehyde	Fisher Chemical	F79500
Dimethylamine borane complex	Millipore Sigma	180238-5G
Deposited data		
*Ab*BamAPOTRA1-4 (P1 space group)	This study	PDB ID: 9CX4
*Ab*BamAPOTRA1-4 ($P3_221$ space group)	This study	PDB ID: 9CX5
Oligonucleotides		
BamA-POTRA1-4 Forward Primer: AGGGCGCCATGGGAGCAGATG ATTTCGTGGTCCG	This paper	N/A
BamA-POTRA1-4 Reverse Primer: GTGGTGCTCGAGTTAACGGCG AACGGTAACCTG	This paper	N/A
Recombinant DNA		
pHis-Parallel2	Sheffield and Derewenda, 1999	N/A
pET20b	Novagen	69739
Software and algorithms		
HKL2000	Otwinowski and Minor, 1997[57]	https://hkl-xray.com/hkl-2000
Phenix	Adams et al., 2010[58]	https://phenix-online.org/
Coot	Emsley et al., 2010[61]	https://www2.mrc-lmb.cam.ac.uk/personal/pemsley/coot/
PyMOL	Schrödinger	https://pymol.org/2/
Photoshop	Adobe	https://www.adobe.com/products/photoshop.html
Illustrator	Adobe	https://www.adobe.com/products/illustrator.html
BioXTAS RAW	Hopkins et al., 2017[62]	https://bioxtas-raw.readthedocs.io/en/latest/
ATSAS	Manalastas-Cantos et al., 2021[63]	https://www.embl-hamburg.de/biosaxs/software.html

EXPERIMENTAL MODEL AND STUDY PARTICIPANT DETAILS

The genes used for cloning originated from *Acinetobacter baumannii* and cloning performed as described in the method details section. The *Escherichia coli* strains used for plasmid propagation and expression in this study are listed in the key resources table. The cells were grown as described in the method details section.

METHOD DETAILS

Cloning

Acinetobacter baumannii BamA (strain ATCC 19606, EnsemblBacteria reference #HMPREF0010_00353) was amplified by polymerase chain reaction (PCR) from a plasmid (pET20b) containing a cassette coding for the entire codon-optimized *A. baumannii* BAM complex (BioBasic). A portion of the BamA gene coding for POTRA 1-4 (amino acids 25-355) was amplified using forward primer 5′- AGGGCGCCATGGGAGCAGATGATTTCGTGGTCCG -3′ and reverse primer 5′- GTGGTGCTCGAGTTAACGGCGAACGGT AACCTG -3'. The BamA POTRA 1-4 insert was then gel extracted (IBI Scientific), restriction enzyme-digested using NcoI and XhoI, and ligated into the pHIS-Parallel2 vector (Novagen). The resulting construct was then verified by DNA sequencing and transformed into BL21(DE3) cells for native protein expression, or the methionine auxotrophic B834(DE3) cells for expression of selenomethionine-substituted BamA POTRA 1-4.

Protein expression and purification

For expression of native BamA POTRA 1-4, a fresh colony was used to inoculate 5 mL of 2xYT containing 100 μg/mL ampicillin, and the culture was grown overnight at 37°C. The next day, the starter culture was washed with 5 mL of fresh 2xYT-Amp, and then subcultured 1:400 into 1 L of fresh 2xYT-Amp. Large-scale cultures were grown with shaking at 37°C to an OD_{600} of 0.5-0.6. The cultures were then induced with 200 μM IPTG and incubated at 20°C overnight. Induced cells were harvested by centrifugation using a JA-14 rotor (Beckman) at 6,000 RPM for 20 min.

The cells were then resuspended in lysis buffer (1x PBS, 10 μg/mL DNase, 200 μM PMSF and 20 mM imidazole) and passed three times through an Avestin Emulsiflex-C3 homogenizer. The lysate was clarified by centrifugation in a JA-20 rotor (Beckman) at 18,000 RPM for 15 min, and the supernatant was collected. Immobilized metal ion affinity chromatography (IMAC) was then performed by applying the soluble supernatants to a 5 mL column packed with HisPur resin (Thermo Scientific) using a PURE FPLC system (GE Healthcare). A linear gradient using Buffer A (1x PBS, 363 mM NaCl and 20 mM imidazole) and Buffer B (1x PBS, 363 mM NaCl and 1 M imidazole) was used to elute BamA POTRA 1-4 from the HisPur column (0–50% Buffer B). Fractions containing BamA POTRA 1-4 were pooled, and the His tag was removed by incubation with TEV protease. Briefly, approximately 1 mg of TEV protease was added to the BamA POTRA 1-4 HisPur fractions (∼1:100 M ratio), and the mixture was dialyzed overnight at 4°C K against 1 L of 1x PBS, 0.5 mM EDTA, and 1 mM DTT. Three dialysis exchanges against 1 L of 1x PBS were performed, and then the BamA POTRA 1-4 TEV cleavage mixture was run over a 5 mL HisPUR column again as an additional reverse-IMAC purification step. The flow through from the reverse-IMAC step containing cleaved BamA POTRA 1-4 was collected and concentrated to 500 μL using a 10 kDa MWCO Amicon centrifugal concentrator (Millipore). SEC was then performed as a final purification step, using a Superdex 200 Increase 10/300 GL column (GE Healthcare) in 1x PBS. Purified BamA POTRA 1-4 was separated on a 4–15% SDS-PAGE gel and visualized using PageBlue Protein Staining Solution (Thermo Scientific).

Expression of selenomethionine-substituted BamA POTRA 1-4 was performed identically to the native protein, only using the Selenomethionine Medium Complete media/nutrient mix system (Molecular Dimensions) containing 40 mg/L L-selenomethionine. Purification of selenomethionine-substituted BamA POTRA 1-4 was identical to the purification of the native protein, except that 1 mM 2-mercaptoethanol was added throughout the purification.

Reductive alkylation of selenomethionine-substituted BamA polypeptide transport associated 1-4

Selenomethionine-substituted *Ab*BamA POTRA 1-4 protein samples were reductively methylated prior to crystallization to increase crystal quality, packing, and size. In brief, 20 μL of 1.0 M dimethylamine borane complex solution and 40 μL of 1.0 M formaldehyde were added to 1 mL of protein at 10 mg/mL, and the mixture was incubated at 4°C for 2 h. Again, 20 μL of 1.0 M dimethylamine borane complex solution and 40 μL of 1.0 M formaldehyde were added to the mixture prior to another 2-h incubation at 4°C. Then, 10 μL of 1.0 M dimethylamine borane complex solution was added and the mixture was incubated overnight at 4°C. The reaction was stopped by adding 125 μL of 1.0 M glycine and 125 μL of 50 mM DTT followed by a 2-h 4°C incubation. As a final step, SEC was performed in 1x PBS prior to crystallization.

Crystallization

For crystallization, BamA POTRA 1-4 was concentrated to 10 mg/mL in 1x PBS for the native protein, or 1x PBS with 1 mM 2-mercaptoethanol for the selenomethionine-substituted protein. Crystallization was performed at 20°C using the hanging drop vapor diffusion method in 96-well trays. Crystal trays were set using a Mosquito LCP (TTP Labtech) crystallization robot. Each hanging drop consisted of 0.2 μL protein solution and 0.2 μL well solution, and drops were equilibrated against 50 μL of well solution.

Commercially available broad-matrix screens were used for high-throughput crystallization screening (hanging drop) using an LCP-Mosquito crystallization robot (SPT Labtech). For native and selenomethionine-substituted samples, condition #49 (0.1 M citric acid, pH 4.0 and 0.8 M ammonium sulfate) from the $AmSO_4$ Suite (Qiagen) produced BamA POTRA 1-4 crystals within a month. Optimization of this condition was then performed by screening chemical conditions around the initial crystallization condition. A Dragonfly (STP Labtech) was used to generate 96-well optimization screens scanning different pHs (3.6 - 4.0) and ammonium sulfate concentrations (0 - 1.6 M). Additionally, an additive screen was performed using the Additive Screen HT (Hampton Research) in an attempt to identify any chemical additives which would improve crystal quality. For the alkylated selenomethionine-substituted

sample, more conditions produced crystals during the initial screening than non-alkylated samples, with final crystals grown in 0.1 M bis-tris propane and 1.2 M DL-malic acid, pH 7.0 (SaltRx HT, #C9; Hampton Research).

Data collection and structure determination

*Ab*BamA POTRA 1-4 crystals were flash-frozen in liquid nitrogen prior to data collection. X-ray diffraction data were collected at beamline 23-ID-B (GM/CA) of the Advanced Photon Source, Argonne National Laboratory, for the native crystals and at beamline 23-ID-D (GM/CA) for the selenomethionine-substituted crystals. Data processing and analysis were performed using HKL-2000[57] and Xtriage.[58] Attempts to phase using molecular replacement were unsuccessful. Therefore, initial phases were calculated using data from the selenomethionine-substituted crystalsin space group $P3_221$ using Se-SAD in AutoSol/PHENIX.[58] Two molecules were observed per asymmetric unit containing a total of 10 selenium sites. The model from Se-SAD phasing was then used as a search model to solve the structure in space group P1 by molecular replacement within PHASER/PHENIX.[58] Model building was performed using Coot[61] and refined using Phenix.[58] Data collection and refinement parameters and results are summarized in Table 1. Structural analysis and figure preparation were performed using PyMOL (Schrödinger). Final figures were assembled using Adobe Photoshop and Illustrator.

Size-exclusion chromatography small angle X-Ray scattering

POTRAs 1-4 from *Ab*BamA (5 mg/mL) were analyzed with SEC-SAXS (Superdex 200 Increase) to analyze its oligomeric state and overall shape. The SEC-SAXS data were collected at the BioCAT beamline at the Advanced Photon Source, Argonne National Laboratory. The data were analyzed and final plots made using BioXTAS RAW v2.2.1[62] and ATSAS.[63] First, the data were reduced, blank subtracted, and data range for scattering curves selected. Upon averaging of the data, the *q*-range and molecular weight information was obtained by Guinier analysis. Pair-distance distribution curves were calculated using GNOM. Theoretical scattering curves for the X-ray structures was calculated and compared with experimental scattering curves using CRYSOL and model refinement performed using the SREFLEX option.

Molecular dynamics simulations

We constructed simulation systems using two chains from the structure resolved here and two chains from *Ec*BamA POTRA domains 1-4 (PDB ID 2QCZ). Each chain was individually placed in a TIP3P water box with sodium (Na^+) and chloride (Cl^-) ions added to achieve a salt concentration of 150 mM. The final system volume was approximately 159 × 159 × 159 $Å^3$ and comprised around 400,000 atoms. Each simulation was conducted for 500 ns.

The simulations were performed using NAMD3[64] with the CHARMM36m[65] force field. Hydrogen mass repartitioning[66] was applied to enable a consistent time step of 4 fs. We maintained the simulations at a constant temperature of 310 K and a pressure of 1 atm using Langevin dynamics and a Langevin piston for temperature and pressure control, respectively.

QUANTIFICATION AND STATISTICAL ANALYSIS

Data collection and refinement statistics for X-ray crystallography are shown in Table 1. The summary of SEC-SAXS parameters is in Table 2.